Catalyst-Free Synthesis of Crumpled Boron and Nitrogen Co-Doped Graphite Layers with Tunable Bond Structure for Oxygen Reduction Reaction

Jutao Jin,[†,‡] Fuping Pan,[†] Luhua Jiang,[‡] Xiaogang Fu,[†] Aiming Liang,[†] Zhiyang Wei,[†] Junyan Zhang,[*,†] and Gongquan Sun[*,‡]

[†]State Key Laboratory of Solid Lubrication, Lanzhou Institute of Chemical Physics, Chinese Academy of Sciences, Lanzhou 730000, People's Republic of China and
[‡]Laboratory of Fuel Cell, Dalian Institute of Chemical Physics, Chinese Academy of Sciences, Zhongshan Road 457, Dalian 116023, People's Republic of China

ABSTRACT Two-dimensional materials based on ternary system of B, C and N are useful ranging from electric devices to catalysis. The bonding arrangement within these BCN nanosheets largely determines their electronic structure and thus chemical and (or) physical properties, yet it remains a challenge to manipulate their bond structures in a convenient and controlled manner. Recently, we developed a synthetic protocol for the synthesis of crumpled BCN nanosheets with tunable B and N bond structure using urea, boric acid and polyethylene glycol (PEG) as precursors. By carefully selecting the synthesis condition, we can tune the structure of BCN sheets from *s*-BCN with B and N bond together to *h*-BCN with B and N homogenously dispersed in BCN sheets. Detailed experiments suggest that the final bond structure of B and N in graphene depends on the preferentially doped N structure in BCN nanosheets. When N substituted the in-plane carbon atom with all its electrons configured into the π electron system of graphene, it facilitates the formation of *h*-BCN with B and N in separated state. On the contrary, when nitrogen substituted the edge-plane carbon with the nitrogen dopant surrounded with the lone electron pairs, it benefits for the formation of B—N structure. Specially, the compound riched with *h*-BCN shows excellent ORR performance in alkaline solution due to the synergistic effect between B and N, while *s*-BCN dominant BCN shows graphite-like activity for ORR, suggesting the intrinsic properties differences of BCN nanosheets with different dopants bond arrangement.

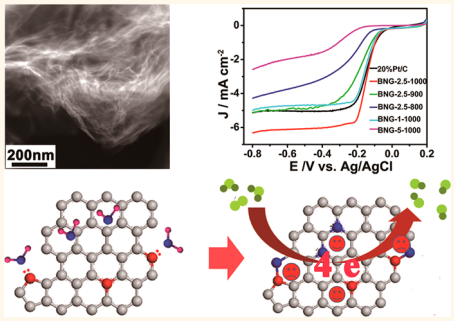

KEYWORDS: catalyst-free · BCN sheet · tunable bond structure · oxygen reduction reaction

Atomic sheets based on ternary system of boron (B), carbon (C) and nitrogen (N) with a graphitic phase (BCN) have recently garnered much interest.[1−12] Compared with graphene and *h*-BN sheets, they are chemically and physically versatile.[13] The electronic structure of BCN, either mono- or few-layered, varies depending on the composition and bonding configuration, enabling a rich variety of properties and applications. The atomic compositions can be tuned in a wide range because of the similar atomic radius of B, C and N atoms.[2,14,15] Furthermore, the atomic configurations of BCN can be a homogeneous single phase of B and N doped graphene (*h*-BCN) or separated domains of *h*-BN in graphene networks (s-BCN).[8,16] The difference of the bonding configuration of B and N in the hybrid makes the property and performance of these two kinds of BCN substantially different. For *h*-BCN, it performs like B and N codoped graphene, in which the extra electron of N and the empty orbital of B can conjugate into carbon system to change the electronic structure or make new electron states, e.g. changing the distribution of electron density and improving the electron spin density.[3,16,17] Upon *s*-BCN, the neutralization of the lone pair electron of N and the empty orbital of B makes them cannot influence the π electron system of graphene. *s*-BCN, with graphene embedded insulating *h*-BN, behaves like porous graphene with abundant nanoholes.[15,18] Previous studies found that BCN nanomaterials, either synthesized by bottom-up CVD method[5,8,12,15,18−21] or top-down

* Address correspondence to zhangjunyan@licp.cas.cn, gqsun@dicp.ac.cn.

Received for review September 21, 2013 and accepted March 6, 2014.

Published online March 06, 2014
10.1021/nn404927n

route[3,22−24] (substituting graphene precursor with B and N by thermal annealing), were prone to form *s*-BCN since the C−C and B−N bonds tend to segregate in the synthesis process. Furthermore, metal catalyst (cobalt or nickel) is used during the common CVD process for the synthesis of BCN sheets, which unavoidably leaves some metal impurities that may affect their properties.[25,26] Lately, a two-step route has been developed to synthesize *h*-BCN with B and N homogeneously doped in graphene lattice. By doping N and B with a separated step, either B[16] or N[17] in priority, one can suppress the formation of *h*-BN segments in graphene grid. Despite these great developments in the synthesis of BCN based nanomaterial, the facile synthesis of BCN with well-defined configuration of B and N remains a challenge. Here, we developed a synthetic protocol for the synthesis of crumpled BCN nanosheets with tunable B and N bond structure using urea, boric acid and polyethylene glycol (PEG) as precursors. Interestingly, we can selectively synthesis *s*-BCN with B and N bond together or *h*-BCN with B and N homogenously dispersed in BCN sheets in a controllable manner.

RESULTS AND DISCUSSION

In a typical synthesis of BCN, a mixture of urea, polyethylene glycol (PEG) and boric acid with a mass ratio of 30:1:0.025 was annealed at 1000 °C in Ar atmospheres at normal pressure (see experimental section for more details). Urea was decomposed and boric acid was dehydrated to afford N and B source, respectively. PEG was carbonized during the heating process to afford carbon source. The basic reactions involved in the formation of B and N dual-doped graphene are shown in the following equation:

$$C + NH_3 + B_2O_3 = BCN + 3H_2O$$

In fact, BCN sheets have been successfully synthesized by annealing urea, boric acid and activated carbon at high temperature.[2] Instead, we use PEG to supersede activated carbon as carbon source. Thus the precursors can be molecularly mixed before heating and react efficiently during the annealing process. To reveal the effect of annealing temperature on the physical and chemical properties of BCN products, the precursor was also annealed at 800 and 900 °C. Figure 1a is a typical transmission electron microscopy (TEM) image of BCN synthesized by annealing urea, PEG and boric acid with a mass ratio of 30:1:0.025 at 1000 °C, showing a crumpled, cross-linked but still transparent thin film. The selected-area electron diffraction (SAED) pattern (Figure 1b) shows that the diffraction ring is consistent with the typical hexagonal pattern of graphene with poor crystallity.[2] Atomic force microscopy (AFM) image (Figure S2) measurement demonstrates that the thickness of most samples are less than 2.1 nm, corresponding to 7 layers according to the theoretical thickness of a single-layer graphene (0.34 nm). The detailed information of the BCN sample was investigated by high-resolution TEM (HRTEM). As shown in Figure 1c, most of the BCN nanosheets are crumpled and contain entangled wrinkles. These layers show a layer distance of about 0.34 nm but with poor crystallity. The crumple structure could be attribute to the local stress induced by the lattice defects, such as vacancies, nitrogen and boron dopants.[27] Figure 1d shows the scanning transmission electron microscopy image of the BCN sample, clearly presenting the entangled and crumpled atomic layers. The element distritution obtained from the area maping indicates the homogenious distritution of B, C, N and O elements. The annealing temperature (>800 °C) has little effect on the morphology of BCN sheet. Fix the mass ratio of urea: PEG: boric acid at 30:1:0.025, samples obtained at 800, 900, and 1000 °C all show crumpled transparent morphology (Figure 1a, Figure S1e, 1f). The specific surface area and the pore structure of the obtained BCN layer sheets were assessed by nitrogen absorption. Gas sorption isotherms (Figure S3a) exhibit typical IV curves, suggesting micromesoporous structure. The BCN-2.5−1000 shows the highest specific surface area of 967 $m^2\ g^{-1}$. The samples obtained at relative low annealing temperature show relatively low specific surface area of 813 $m^2\ g^{-1}$ and 759 $m^2\ g^{-1}$ for BCN-2.5−900 and BCN-2.5−800, respectively. The high annealing temperature may facilitate the etching of the amorphous carbon and thus lead to a high surface area. The pore radius distributions of all samples are centered at about 2.8 nm (Figure S3b), which suggests the unchanged pore structure with annealing temperature. Compared with annealing temperature, the mass ratio of precursor can significantly affect the morphology of BCN sheet. A high mass ratio of urea to PEG is necessary for the synthesis of few layered BCN. Samples prepared with or without a low mass ratio of urea to PEG show bulk graphite morphology (Figure S1a and S1g). This phenomenon may be resulted from the fact that urea can produce a large volume of gaseous species during the heating process, which is favorable for the formation of a few layered BCN sheets. The optimized mass ratio of urea to PEG was found to be 30:1. Boric acid can also affect the morphology of BCN sheets. Fixed the mass ratio of urea to PEG at 30:1, the size of BCN layers produced without or with little amount of boric acid (Figure S1b, S1c and S1h) are smaller than that of with higher boric acid content. Boric acid has two functions in the formation of uniform BCN sheets. Besides affording B source for B doping, we propose that boric acid may be converted to boric oxide to wrap the newly formed nanographene during the synthesis process, which reduces the surface energy and suppresses their aggregation to bulk graphite phase. Similar phenomenon has also been reported in the procedure for the synthesis of

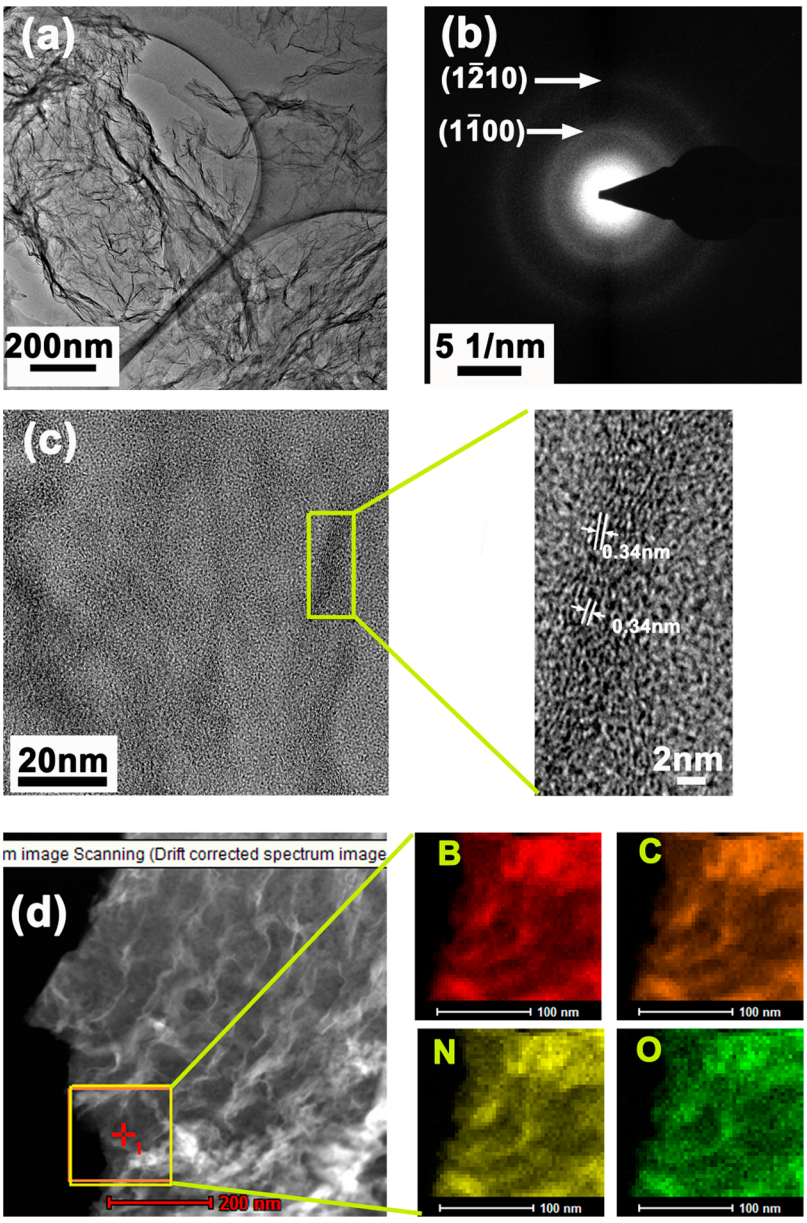

Figure 1. (a) TEM image of BCN-2.5−1000 and (b) the corresponding selected-area electron diffraction pattern; (c) HRTEM image of BCN-2.5−1000 and HRTEM of crumple zone in c; (d) STEM image of BCN-2.5−1000 and the distribution of B, C, N, and O elements.

BCN nanotube during which boric acid could hinder the aggregation of carbon nanotube by wrapping them during the heating process.[23] In the following in this paper, with the mass ratio of urea, PEG and boric acid varied at 30:1:0.01, 30:1:0.025, 30:1:0.1, the samples are labeled as BCN-1-T, BCN-2.5-T and BCN-5-T, respectively, where T refers to the annealing temperature.

X-ray photoelectron spectroscopy (XPS) were conducted to reveal the content of B and N in BCN. XPS spectra show the presence of B, C, N and O in all samples. The content of each element calculated from their relative intensity are listed in table 1. The composition of BCN strongly depends on the synthesis temperature. Both the contents of B and N decrease with increasing the annealing temperature, indicating that B and N dopants may become unstable and is removed from the BCN crystal lattice at elevated temperature.[28] This result is confirmed by roman spectra (Figure S6) that BCN annealed at higher temperature shows higher intensity ratio of D (I_D) to G band (I_G), I_D/ I_G. The precursor ratio can also intensively affect the final composition of BCN products. As shown in Table 1, the N content increases from5.64 ± 0.23 at. % for BCN-1−1000 to 9.47 ± 1.14 at. %. for BCN-5−1000, B content increases together with N from 1.23 ± 0.19 at. % for BCN-1−1000 to 7.76 ± 1.03 at. % for BCN-5−1000. In fact, when N, with a smaller atomic radius than that of C, is doped into graphene lattice, it may facilitate B doping by counteracting the N induced lattice pressure stress, and *vice versa*.

TABLE 1. Distribution of Element Species Obtained from the De-convolution of the B1s, C1s, N1s, and O1s Peaks by XPS

		atom %				
entry	binding energy (eV)	BNG-1−1000	BNG-2.5−1000	BNG-5−1000	BNG-2.5−900	BNG-2.5−800
total C		88.65 ± 1.17	82.62 ± 1.83	80.05 ± 2.31	79.20 ± 0.98	75.83 ± 1.81
total O		4.48 ± 0.56	4.21 ± 0.34	3.70 ± 0.88	4.33 ± 0.56	4.25 ± 0.43
total N		5.64 ± 0.23	8.79 ± 1.17	9.47 ± 1.14	11.10 ± 1.74	13.07 ± 1.98
N1	402.3 ± 0.2	0.19 ± 0.09	0.63 ± 0.09	0.86 ± 0.06	1.34 ± 0.18	0.90 ± 0.08
N2	400.6 ± 0.2	3.09 ± 0.17	4.56 ± 0.93	1.10 ± 0.09	2.92 ± 0.09	2.37 ± 0.17
N3	399.6 ± 0.2	1.79 ± 0.11	0.64 ± 0.07	0.82 ± 0.04	1.42 ± 0.12	3.19 ± 0.32
N4	398.7 ± 0.2	0.19 ± 0.05	2.08 ± 0.61	2.94 ± 0.07	3.56 ± 0.89	2.59 ± 0.47
N5	397.6 ± 0.2	0.38 ± 0.07	0.89 ± 0.07	3.76 ± 1.01	1.86 ± 0.09	4.03 ± 1.01
total B		1.23 ± 0.19	4.38 ± 0.87	7.76 ± 1.03	5.37 ± 0.97	6.85 ± 1.03
B1	189.6 ± 0.2	0.45 ± 0.07	1.73 ± 0.12	2.02 ± 0.43	2.07 ± 0.61	1.55 ± 0.21
B2	191.2 ± 0.2	0.40 ± 003	1.12 ± 0.21	3.90 ± 0.67	2.12 ± 0.87	4.23 ± 0.89
B3	192.6 ± 0.2	0.38 ± 0.06	1.53 ± 0.27	1.83 ± 0.32	1.11 ± 0.31	1.07 ± 0.11

High resolution XPS spectra were conducted to reveal the bonding configurations of all BCN samples (Figure 2). The N1s band can be deconvoluted into five bands at 397.6, 398.7, 399.6, 400.6, and 402.3 eV, assigned to N atoms as B−N (N5), pyridinic C−N (N4), pyrrollic C−N (N3), grapitic C−N (N2) and oxidic O−N (N1) structure, respectively.[29,30] The B1s band can be deconvoluted into three bands at 189.6, 191.2, and 192.6 eV, corresponding to the C−B (B3), N−B (B2) and O−B (B1) bonding structures, respectively.[29] The molecular bonding structures of each dopant are depicted clearly (Figure 2b) and their concentration are summarized in table 1. As mentioned above, two kinds of BCN, *s*-BCN and *h*-BCN, are formed during the synthesis process. For simple, we assign C−B and graphitic C−N bonding structure as *h*-BCN phase, while the B−N bonding as *s*-BCN phase. By calculating the content of these bonding configurations, we get the fraction of each phase in the sample. From Figure 2a and 2b, it can be seen that, for BCN-2.5−800, both N1s and B1s band show the presence of a large amount of B−N bonding, while the C−N and C−B are negligible, suggesting that *s*-BCN phase dominates BCN-2.5−800. Upon BCN-2.5−900, the bands corresponding to B−N become weaker in both B1s and N1s spectra, while the bands belong to C−N and C−B become much stronger. Upon further increasing the annealing temperature for BCN-2.5−1000, the intensity of the B−N peak becomes much weaker and its proportion is obviously smaller than that of BCN-2.5−900 and BCN-2.5−800, whereas the peaks of B−C and C−N rose largely, indicating that BCN-2.5−1000 is mainly composed of *h*-BCN. During the formation of BCN nanosheets, urea was decomposed to produce components like cyanuric acid, ammelide and melamine at low temperature (about 350 °C), which were polymerized to form *g*-C_3N_4 at a relatively higher temperature (about 550 °C).[28,31,32] Along with this procedure, the PEG was carbonized to form carbon with poor crystallinity between *g*-C_3N_4 nanosheets. At temperature above 600 °C, the *g*-C_3N_4 from urea was decomposed to supply abundant nitrogen-containing gaseous species, accompanied with which the porous thin graphite layer is formed and nitrogen species are doped into the porous carbon. As a matter of fact, the *in situ* formed g-C_3N_4 functioned as soft-template during the forming of graphite layer sheet. Compared with N, B is more difficult to dope into the graphite lattice during the annealing process.[33] In fact, boric acid is more stable than urea during the annealing process. It first transforms into boric oxide at temperature about 300 °C,[34] and then into active radical, e.g. B_2O_2(g), at elevated temperature (above 900 °C).[35,36] In addition, the mismatch between B and C is larger than that of N and C in graphite lattice. These two reasons together make that the doping process of B is kinetically slower than that of N. As shown in Figure 2e, with annealing temperature increase from 800 to 1000 °C, the content of C−N and C−B increases while B−N decreases for sample BCN-2.5, suggesting it is more favorable for the formation of *h*-BCN at high temperature while *s*-BCN at low temperature. This phenomenon can be explained from the view of atomic structure (Figure 2d). It has been reported that N is prone to form edge-N (pyrindinic-N and pyrollic-N) at low temperature for nitrogen doped carbon.[37] These edge-N with unpaired electrons tend to bond with B to form B−N structure. While at higher temperature, graphitic-N are dominant nitrogen species.[37] The lone electron pairs of nitrogen are conjugated into the carbon electron system, leaving no unpaired electrons to bond with B. This means that the final bonding structure of B and N in BCN nanosheets is determined by the preferentially doped N structure in the nanosheet. As a matter of fact, *h*-BCN corresponds to B and N atoms homogeneously doped in BCN sheets is more favorable "entropically" than s-BCN with BN domains separated in BCN sheets, since *h*-BCN is more disordered than *s*-BCN. On the contrary, *s*-BCN is more favorable "enthalpically" than h-BCN since $\varepsilon(B-N)>1/2(\varepsilon(X-N)+\varepsilon(X-B))$, where $\varepsilon(B-N)$,

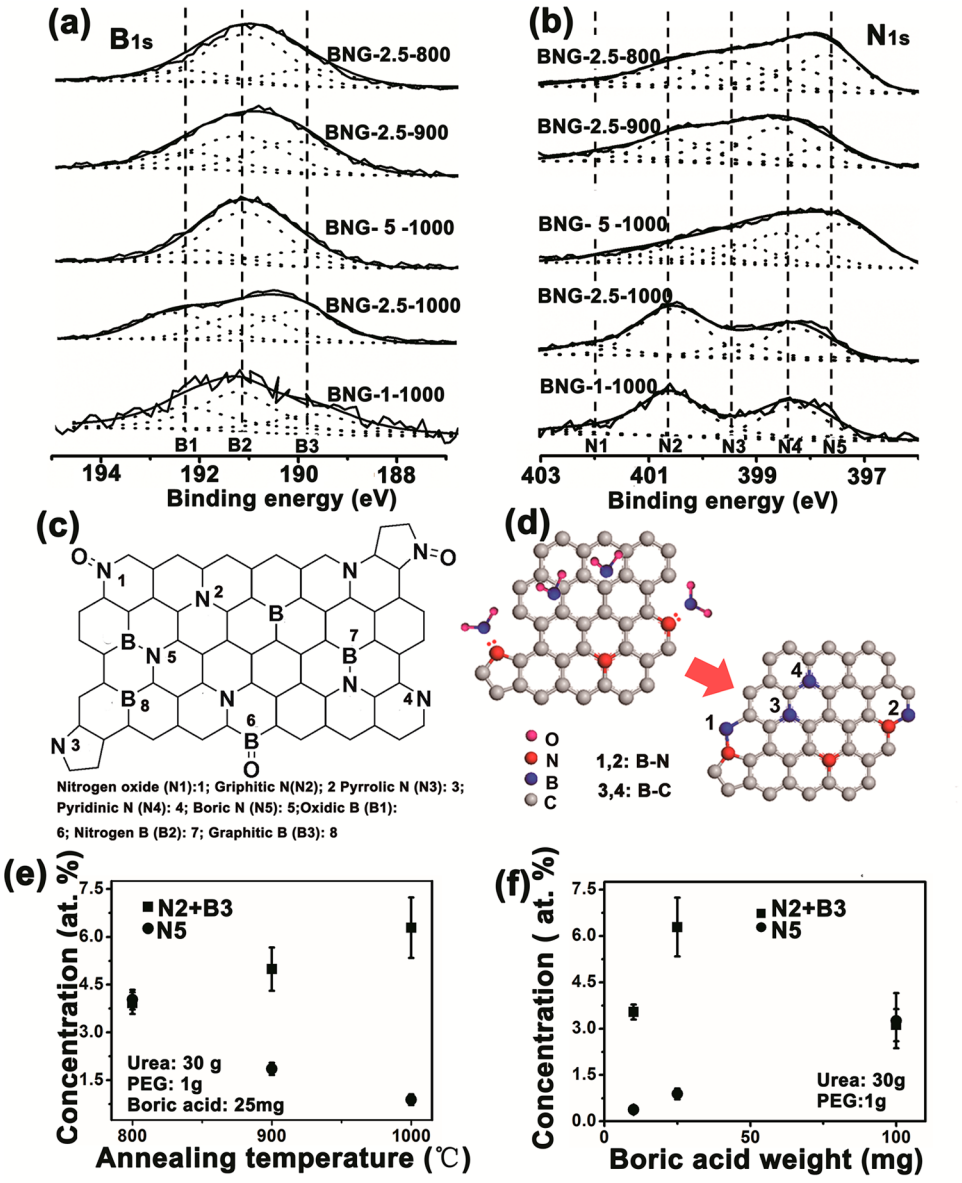

Figure 2. (a) B1s and (b) N1s XPS spectra of BCN samples; (c) schematic of possible bonding configurations for B and N atoms in BCN; (d) B−N bond structure formation mechanism at the edge of the dynamic layer of a growing BCN sheet; (e) B3 and N2 content and N1 content vs synthesis temperature (*T*) (BCN-2.5), (f) B3 plus N2 content vs boric acid weight and N1 content vs boric acid weight.

ε(C−N) and ε(C−B) refers to bond energy of B−N, C−N and C−B, respectively.[33] In fact, the production of h-BCN or s-BCN is a competition between the formation of C−B (C−N) and B−N bonding configurations to achieve the minimum Gibbs free energy (G). At high temperature, *h*-BCN is energetically favorable since the distribution of the B and N atoms is predominantly determined by entropy. While at low temperature, the distribution of B and N atoms is predominantly determined by enthalpy, in this case, *s*-BCN is more energetically favorable. However, this phenomenon is only observed in suitable precursor mass ratio range. As shown in Figure 2f, for the sample of BCN-5 with higher boric acid ratio, a large amount of *s*-BCN is formed even at high temperature of 1000 °C.For BCN-1−1000 with lower boric acid ratio, it is mainly composed of *h*-BCN but with less C−N and C−B content compared with BCN-2.5−1000.

It has been reported that hybrid carbon materials, including carbon nanotube and graphene, show high oxygen reduction reaction (ORR) activity.[3,16,17,20,38−42] Here, we study the ORR performance of all BCN samples. Figure 3a depicts the cyclic voltammograms (CV) for oxygen reduction on BCN-2.5−1000 modified glassy carbon electrode (red line), as compared to a commercial Pt/C catalyst (black line) as a reference (20 wt % platinum on carbon black). For the Ar-saturated solution, reduction peaks are negligible both for BCN-2.5−1000 (red dash line) and Pt/C (black dash line). In the presence of oxygen, an obvious reduction

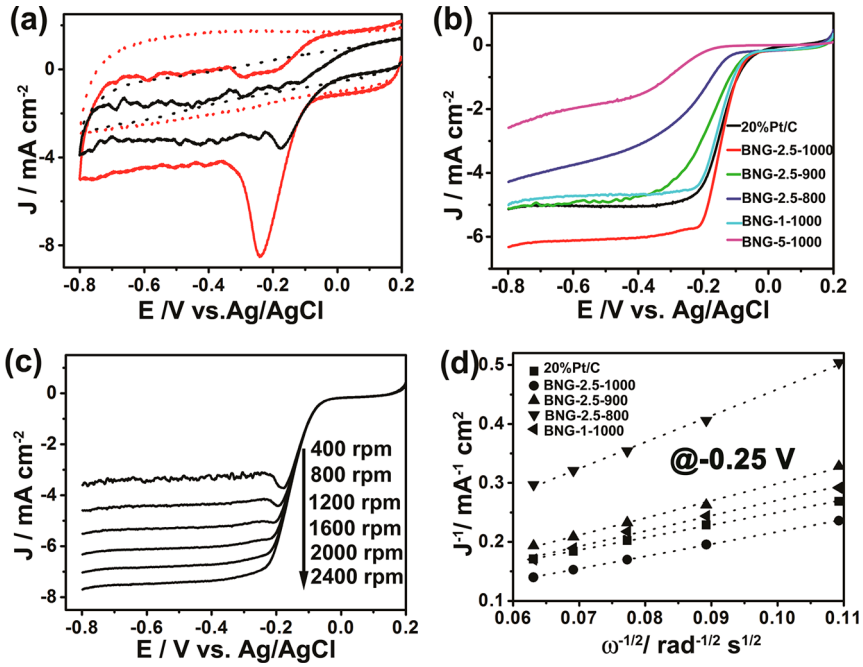

Figure 3. (a) Cyclic voltammograms for BCN-2.5−1000 (red) and Pt/C (black) on a glassy carbon rotating disk electrode saturated in O_2 (solid line) and Ar (dash line) with scan rate of 50 mV s^{-1}.; (b) Rotating-disk voltammograms of various BCN samples in O_2-saturated 0.1 M KOH with a scan rate of 10 mV s^{-1} and rotation rate of 1600 rpm. (c) Rotating-disk voltammograms of BCN-2.5−1000 in O_2-saturated 0.1 M KOH with a sweep rate of 5 mVs^{-1} at the different rotation rates indicated. (d) K−L plots at −0.25 V for the ORR of various BCN samples and commerical 20% Pt/C catalyst.

peak appears around −0.23 V along with a peak current density of 8.3 mA cm^{-2}, compared with −0.19 V and 3.9 mA cm^{-2} for Pt/C. These results demonstrate the excellent ORR performance of BCN-2.5−1000.

To reveal the active sites of BCN for ORR, the samples prepared were mounted on rotating disk electrode (RDE) and tested in O_2 saturated 0.1 M KOH solution with a scanning rate of 10 mV s^{-1}. Figure 3b shows the ORR polarization curves obtained at a rotation rate of 1600 rpm, from which we got the onset (E_0) and half-wave potentials ($E_{1/2}$) and the results were listed in Table S1. E_0 and $E_{1/2}$ are 47 and −147 mV, respectively, for the sample BCN-2.5−1000, similar to that of Pt/C. The result is better than most of recently reported metal free heteroatom doped carbons, including B and N codoped nanocarbons.[3,16,17,20,39−42] Compared with BCN-2.5−1000, BCN-1−1000 and BCN-2.5−900 exhibit similar onset and half-wave potential, suggesting BCN-2.5−1000, BCN-1−1000 and BCN-2.5−900 contain similar intrinsic active sites for ORR. Upon BCN-2.5−800 and BCN-5−1000, their ORR performances are very similar to undoped carbon itself, thus indicating that the ORR process on these catalysts are mainly an inefficient two-electron reduction O_2 to peroxide. BCN-2.5−1000, BCN-1−1000 and BCN-2.5−900 are mainly composed of *h*-BCN. The B and N in these samples are mostly in separated state, which prevents the neutralization between the electron acceptor (B) and electron donor (N) to maintain their intrinsic doping nature. Thus, the electronic sturcture of BCN can be modulated, e.g. enhanced atomic spin dentisy and electron density near the Fermi level, induced by the host−guest electronic interaction.[20] While for BCN-2.5−800 and BCN-5−1000, s-BCN is dominant. The electrtons provided by N are combined with the empty oribtals provided by B, leaving no electron or empty orbital conjugate into carbon system. These intrinsic different nature of B and N in BCN nanosheets can account for the large disparity in their ORR performance.

RDE measurements at varied rotation rate were carried out to reveal the ORR kinetics of the BCN for ORR (Figure 3b and Figure S6). The corresponding Koutecky−Levich (K−L) plots show the inverse current density (j^{-1}) as a function of the inverse of the square root of the rotation speed ($\omega^{-1/2}$) (Figure 3d). All samples show a linear K-L plots at −0.25 V, suggesting the first order reaction kinetics toward the concentration of O_2. The electron transfer number (n) and the kinetic-limiting current density (J_k), two important parameters that reflect the kinetics of ORR process, are calculated from the slope and the reciprocal of the intercept of the K-L plots, respectively (See experimental section for the details of the calculation of J_k and n). For BCN-2.5−1000, the K-L plot is nearly parallel to that of Pt/C, indicating that the ORR is dominated by a four-electron process like Pt/C. Similarly, the electron transfer number of BCN-2.5−900 and BCN-1−1000 are calculated to be 3.65 and 3.77, respectively, thus revealing that these samples still favor a 4-e ORR process. Nevertheless, the J_k value of BCN-2.5−1000 is 26.62 mA cm^{-2}, which is much larger than that

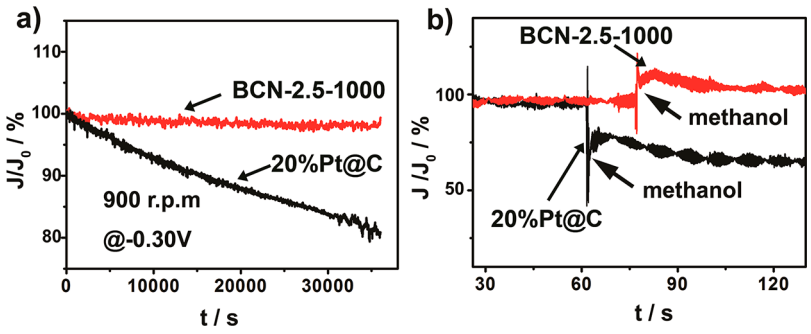

Figure 4. (a) Chronoamperometry of BCN-2.5−1000 and Pt/C electrodes in O_2-saturated 0.1 M KOH at −0.30 V for 10 h. (b) Chronoamperometric responses of BCN-2.5−1000 and Pt/C electrodes with 2 M methanol added.

of BCN-2.5−900 (15.73 mA cm^{-2}), BCN-1−1000 (16.89 mA cm^{-2}) and Pt/C (17.97 mA cm^{-2}). The large J_k value of BCN-2.5−1000 may originate from its higher B and N contents. For BCN-2.5−800 and BCN-5−1000, calculated n value is about 2, revealing a mainly 2-e ORR process. It should be noted that the ORR performance of BCN-2.5−1000 is better than most of recently reported electrocatalyst in terms of onset potential, half-wave potential as well as kinetic current density-(Table S1). The intrinsic properties of the h-BCN layer sheet induced by the synergetic effect of B and N, together with the high specific surface area and the nature of crumpled structure of the layer sheet, endows the materials a high oxygen reduction catalytic performance.

The durability of BCN-2.5−1000 and Pt/C catalysts toward ORR was evaluated through chronoamperometric measurements at −0.4 V. As shown in Figure 4a, the 10 h test only caused a slight activity loss on BCN-2.5−1000 catalyst, whereas Pt/C lost nearly 20% of its initial activity. These results indicate a much better stability of BCN-2.5−1000 catalyst than commercial Pt/C catalyst in alkaline solution. We further test methanol tolerate ability of BCN-2.5−1000 and Pt/C catalysts by adding 5 mL methanol to 25 mL 0.1 M KOH elctrolyte . After adding methanol to the electrolyte, the current density of Pt/C catalyst shows a sharp loss of 40% in activity, whereas BCN-2.5−1000 catalyst retained stable current response. These results clearly show the better catalytic tolerance of BCN-2.5−1000 catalyst and its suitability as a cathode catalyst for alkaline fuel cells than the commercial Pt/C catalyst.

CONCLUSIONS

In summary, we have achieved the catalyst-free bottom-up CVD synthesis of BCN sheets by thermally decomposing solid B-, C- and N-containing precursors at normal pressure. Significantly, the B and N configurations can be easily tuned to form *s*-BCN or *h*-BCN dominant BCN in suitable precursor mass ratio range by simply change the synthesis temperature. The compound riched with *h*-BCN shows excellent ORR performance in alkaline solution because of the synergistic effect between B and N, while *s*-BCN dominant BCN shows intrinsic graphite-like activity for ORR. This method provides not only an effective approach for fabricating BCN that is cheap yet of high quality but also a new concept to control the B and N bonding configurations in BCN.

EXPERIMENTAL SECTION

Synthesis of BCN. To prepare BCN nanosheets, urea (30 g), PEG (1 g), and boric acid (0.025 g) were dissolved in water by sonicating for 30 min. Then the mixture was heated to 80 °C and stirred in 250 mL beaker until a sticky mixture was obtained. The as obtained samples were put in a covered crucible in the center of a tube furnace. Then, the furnace was pumped with rotary pump and washed with Ar for three times to remove oxygen in the tube furnace completely. Then, the temperature of the furnace was rapidly raised to an appointed temperature with a heating rate of 5 °C min^{-1} and annealed for 5 h for preparation BCN-2.5 sheet in Ar atomosphere. Three annealing temperature of 800, 900, and 1000 °C were chosen to synthesize BCN-2.5−800, BCN-2.5−900 and BCN-2.5−1000, respectively.

BCN-1−1000 and BCN-5−1000 with different precursor mass ratio of boric acid were prepared by the same procedure.

Electrochemical Test. The electrochemical tests were carried out on an AutoLab workstation. Electrochemical measurements were conducted using a three-electrode electrochemical cell. The loading of the catalyst on glassy carbon electrode and the measurement of their electrochemical properties as followed procedures similar to our previously reported work.[43] Simply, a glass carbon electrode coated with catalysts attached to a rotating ring disk electrode was used as working electrode. The catalysts coated electrode was prepared as follows: 100 μL of 5 wt % Nafion solution was added in 1 mL of 4:1 v/v water/ethanol, and then 4 mg of catalyst was dispersed in the as prepared solution by at least 60 min sonication to form a homogeneous suspension. Then 5 μL of the suspension was loaded onto a glass carbon electrode of 3 mm in diameter with a mass loading of about 0.283 mg cm^{-2}. The catalyst inks were dried at room temperature. A Ag/AgCl electrode in saturated KCl aqueous solution (with a nominal potential of 0.197 V versus reversible hydrogen electrode) and a platinum wire were used as reference and counter electrode, respectively. The electrolyte comprised a 0.1 M aqueous KOH. All catalysts were activated by 20 cycles of cyclic voltammetry (CV) with a 50 mV s^{-1} scan rate from 0.2 to −0.8 V (vs Ag/AgCl) in Ar-saturated 0.1 M KOH electrolyte before experiments. The linear sweep voltammetry was obtained at a scan rate of 10 mV s^{-1} in the potential range of 0.2 V- −0.8 V (0.1 KOH). In the ORR experiment, the electrolyte was bubbled with high-purity O_2 for 30 min before each test and maintained under atmosphere with constant O_2 gas

flow during the measurements. Long-term stability test of a BCN-2.5−1000 catalyst at a constant voltage of −0.4 V in O_2 bubbled 0.1 M KOH electrolytes. All experiments were conducted at room temperature (20 °C).

RDE measurement. The Koutecky−Levich equation is listed as in eq 1.

$$J_{measured}^{-1} = J_{\infty}^{-1} + J_k^{-1}$$
$$J_{\infty} = 0.62FD_{oxygen}^{2/3}\upsilon^{1/6}C_{oxygen}n\omega^{1/2} = Kn\omega^{1/2} \quad (1)$$
$$K = 0.62FD_{oxygen}^{2/3}\omega^{1/6}C_{oxygen}$$

where F is the Faradaic constant, D_{oxygen} is the O_2 diffusion coefficient in the electrolyte, υ is the kinematic viscosity in the electrolyte, C_{oxygen} is the O_2 saturation concentration in the electrolyte, n is the number of electrons, and ω is the disk electrode rotation rate. K reflects the physical-chemical parameter of the electrolyte. Instead of calculating K value by referring to references electrolyte constant (D_{oxygen}, υ), which highly depends on experimental conditions (such as temperature), we estimated K value by calculating the slope of Koutecky−Levich plot(K_{pt}) of the ORR on the Pt electrode at −0.25 V in oxygen saturated 0.1 M KOH (Figure S6), which was assumed to undergo the direct four-electron transfer process eq 2.

$$J_{measured}^{-1} = K_{pt}\omega^{-1/2} + J_k^{-1}$$
$$K = 1/(nK_{pt}) \quad (2)$$
$$n = 4$$

Then, the slope ($K_{BCN\text{-}2.5-1000}$) and intercept ($Q_{BCN\text{-}2.5-1000}$) of BCN-2.5−1000 hybrid at different potential were calculated from the Koutecky−Levich equation (eq. S1). The electron transfer number (n) and kinetic-limited current density (J_k) of BCN-2.5−1000 at different potential were obtained by eq 3.

$$n = 1/(KK_{BCN\text{-}2.5-1000})$$
$$J_k = -Q_{BCN\text{-}2.5-1000}^{-1} \quad (3)$$

Conflict of Interest: The authors declare no competing financial interest.

Acknowledgment. We acknowledge Prof. Y. Peng of Lanzhou University for the TEM test. We also acknowledge Prof. L. He and L. Gao at Lanzhou Institute of Chemical Physics, Chinese Academy of Sciences, for XRD and XPS measurements, respectively.

Supporting Information Available: Figures S1−S6 and Table S1. This material is available free of charge *via* the Internet at http://pubs.acs.org.

REFERENCES AND NOTES

1. Kim, S. M.; Hsu, A.; Araujo, P. T.; Lee, Y.-H.; Palacios, T.; Dresselhaus, M.; Idrobo, J.-C.; Kim, K. K.; Kong, J. Synthesis of Patched or Stacked Graphene and h-BN Flakes: A Route to Hybrid Structure Discovery. *Nano Lett.* **2013**, *13*, 933–941.
2. Raidongia, K.; Nag, A.; Hembram, K.; Waghmare, U. V.; Datta, R.; Rao, C. N. R. BCN: A Graphene Analogue with Remarkable Adsorptive Properties. *Chem.—Eur. J.* **2010**, *16*, 149–157.
3. Wang, S.; Zhang, L.; Xia, Z.; Roy, A.; Chang, D. W.; Baek, J.-B.; Dai, L. BCN Graphene as Efficient Metal-Free Electrocatalyst for the Oxygen Reduction Reaction. *Angew. Chem., Int. Ed.* **2012**, *51*, 4209–4212.
4. Lei, W.; Qin, S.; Liu, D.; Portehault, D.; Liu, Z.; Chen, Y. Large Scale Boron Carbon Nitride Nanosheets with Enhanced Lithium Storage Capabilities. *Chem. Commun.* **2013**, *49*, 352–354.
5. Levendorf, M. P.; Kim, C.-J.; Brown, L.; Huang, P. Y.; Havener, R. W.; Muller, D. A.; Park, J. Graphene and Boron Nitride Lateral Heterostructures for Atomically Thin Circuitry. *Nature* **2012**, *488*, 627–632.
6. Sutter, P.; Cortes, R.; Lahiri, J.; Sutter, E. Interface Formation in Monolayer Graphene-Boron Nitride Heterostructures. *Nano Lett.* **2012**, *12*, 4869–4874.
7. Jung, J.; Qiao, Z.; Niu, Q.; MacDonald, A. H. Transport Properties of Graphene Nanoroads in Boron Nitride Sheets. *Nano Lett.* **2012**, *12*, 2936–2940.
8. Stephan, O.; Ajayan, P. M.; Colliex, C.; Redlich, P.; Lambert, J. M.; Bernier, P.; Lefin, P. Doping Graphitic and Carbon Nanotube Structures with Boron and Nitrogen. *Science* **1994**, *266*, 1683–1685.
9. Wu, Z.-S.; Winter, A.; Chen, L.; Sun, Y.; Turchanin, A.; Feng, X.; Müllen, K. Three-Dimensional Nitrogen and Boron Co-doped Graphene for High-Performance All-Solid-State Supercapacitors. *Adv. Mater.* **2012**, *23*, 5130–5134.
10. Sun, Z.; Yan, Z.; Yao, J.; Beitler, E.; Zhu, Y.; Tour, J. M. Growth of Graphene From Solid Carbon Sources. *Nature* **2010**, *468*, 549–552.
11. Liu, Z.; Ma, L.; Shi, G.; Zhou, W.; Gong, Y.; Lei, S.; Yang, X.; Zhang, J.; Yu, J.; Hackenberg, K. P.; et al. In-Plane Heterostructures of Graphene and Hexagonal Boron Nitride with Controlled Domain Sizes. *Nat. Nanotechnol.* **2013**, *8*, 119–124.
12. Iyyamperumal, E.; Wang, S.; Dai, L. Vertically-Aligned BCN Nanotubes with High Capacitance. *ACS Nano* **2012**, *6*, 5259–5265.
13. Song, L.; Liu, Z.; Reddy, A. L. M.; Narayanan, N. T.; Taha-Tijerina, J.; Peng, J.; Gao, G.; Lou, J.; Vajtai, R.; Ajayan, P. M. Binary and Ternary Atomic Layers Built from Carbon, Boron, and Nitrogen. *Adv. Mater.* **2012**, *24*, 4878–4895.
14. Yin, L.-W.; Bando, Y.; Golberg, D.; Gloter, A.; Li, M.-S.; Yuan, X.; Sekiguchi, T. Porous BCN Nanotubular Fibers: Growth and Spatially Resolved Cathodoluminescence. *J. Am. Chem. Soc.* **2005**, *127*, 16354–16355.
15. Ci, L.; Song, L.; Jin, C.; Jariwala, D.; Wu, D.; Li, Y.; Srivastava, A.; Wang, Z. F.; Storr, K.; Balicas, L.; et al. Atomic Layers of Hybridized Boron Nitride and Graphene Domains. *Nat. Mater.* **2010**, *9*, 430–435.
16. Zheng, Y.; Jiao, Y.; Ge, L.; Jaroniec, M.; Qiao, S. Z. Two-Step Boron and Nitrogen Doping in Graphene for Enhanced Synergistic Catalysis. *Angew. Chem., Int. Ed.* **2013**, *125*, 3110–3116.
17. Zhao, Y.; Yang, L.; Chen, S.; Wang, X.; Ma, Y.; Wu, Q.; Jiang, Y.; Qian, W.; Hu, Z. Can Boron and Nitrogen Co-Doping Improve Oxygen Reduction Reaction Activity of Carbon Nanotubes? *J. Am. Chem. Soc.* **2013**, *135*, 1201–1204.
18. Chang, C.-K.; Kataria, S.; Kuo, C.-C.; Ganguly, A.; Wang, B.-Y.; Hwang, J.-Y.; Huang, K.-J.; Yang, W.-H.; Wang, S.-B.; Chuang, C.-H.; et al. Band Gap Engineering of Chemical Vapor Deposited Graphene by *in situ* BN Doping. *ACS Nano* **2012**, *7*, 1333–1341.
19. Wu, T.; Shen, H.; Sun, L.; Cheng, B.; Liu, B.; Shen, J. Nitrogen and Boron Doped Monolayer Graphene by Chemical Vapor Deposition Using Polystyrene, Urea and Boric Acid. *New J .Chem.* **2012**, *36*, 1385–1391.
20. Wang, S.; Iyyamperumal, E.; Roy, A.; Xue, Y.; Yu, D.; Dai, L. Vertically Aligned BCN Nanotubes as Efficient Metal-Free Electrocatalysts for the Oxygen Reduction Reaction: A Synergetic Effect by Co-Doping with Boron and Nitrogen. *Angew. Chem., Int. Ed.* **2011**, *50*, 11756–11760.
21. Li, X.-H.; Antonietti, M. Polycondensation of Boron- and Nitrogen-Codoped Holey Graphene Monoliths from Molecules: Carbocatalysts for Selective Oxidation. *Angew. Chem., Int. Ed.* **2013**, *52*, 4572–4576.
22. Lin, T.-W.; Su, C.-Y.; Zhang, X.-Q.; Zhang, W.; Lee, Y.-H.; Chu, C.-W.; Lin, H.-Y.; Chang, M.-T.; Chen, F.-R.; Li, L.-J. Converting Graphene Oxide Monolayers into Boron Carbonitride Nanosheets by Substitutional Doping. *Small* **2012**, *8*, 1384–1391.
23. Yang, X.; Liu, L.; Wu, M.; Wang, W.; Bai, X.; Wang, E. Wet-Chemistry-Assisted Nanotube-Substitution Reaction for High-Efficiency and Bulk-Quantity Synthesis of Boron- and Nitrogen-Codoped Single-Walled Carbon Nanotubes. *J. Am. Chem. Soc.* **2011**, *133*, 13216–13219.
24. Paul, R.; Voevodin, A. A.; Zemlyanov, D.; Roy, A. K.; Fisher, T. S. Microwave-Assisted Surface Synthesis of a Boron−Carbon−Nitrogen Foam and its Desorption Enthalpy. *Adv. Funct. Mater.* **2012**, *22*, 3682–3690.
25. Ambrosi, A.; Chua, C. K.; Khezri, B.; Sofer, Z.; Webster, R. D.; Pumera, M. Chemically Reduced Graphene Contains

Inherent Metallic Impurities Present in Parent Natural and Synthetic Graphite. *Proc. Nat. Acad. Sci. U.S.A.* **2012**, *109*, 12899–12904.
26. Ambrosi, A.; Chee, S. Y.; Khezri, B.; Webster, R. D.; Sofer, Z.; Pumera, M. Metallic Impurities in Graphenes Prepared from Graphite Can Dramatically Influence Their Properties. *Angew. Chem., Int. Ed.* **2012**, *51*, 500–503.
27. Paredez, P.; Maia da Costa, M. E. H.; Zagonel, L. F.; Ribeiro, C. T. M.; Alvarez, F. Growth of Nitrogenated Fullerene-Like Carbon on Ni Islands by Ion Beam Sputtering. *Carbon* **2007**, *45*, 2678–2684.
28. Jin, J.; Fu, X.; Liu, Q.; Liu, Y.; Wei, Z.; Niu, K.; Zhang, J. Identifying the Active Site in Nitrogen-Doped Graphene for the VO^{2+}/VO_2^{+} Redox Reaction. *ACS Nano* **2013**, *7*, 4764–4773.
29. Kim, S. Y.; Park, J.; Choi, H. C.; Ahn, J. P.; Hou, J. Q.; Kang, H. S. X-ray Photoelectron Spectroscopy and First Principles Calculation of BCN Nanotubes. *J. Am. Chem. Soc.* **2007**, *129*, 1705–1716.
30. Wang, H.; Maiyalagan, T.; Wang, X. Review on Recent Progress in Nitrogen-Doped Graphene: Synthesis, Characterization, and Its Potential Applications. *ACS Catal.* **2012**, *2*, 781–794.
31. Zou, X.-X.; Li, G.-D.; Wang, Y.-N.; Zhao, J.; Yan, C.; Guo, M.-Y.; Li, L.; Chen, J.-S. Direct Conversion of Urea into Graphitic Carbon Nitride over Mesoporous TiO_2 Spheres under Mild Condition. *Chem. Commun.* **2011**, *47*, 1066–1068.
32. Liu, J.; Zhang, Y.; Lu, L.; Wu, G.; Chen, W. Self-Regenerated Solar-Driven Photocatalytic Water-Splitting by Urea Derived Graphitic Carbon Nitride with Platinum Nanoparticles. *Chem. Commun* **2012**, *48*, 8826–8828.
33. Liu, Z.; Marder, T. B. B−N *versus* C−C: How Similar Are They? *Angew. Chem., Int. Ed.* **2008**, *47*, 242–244.
34. Sevim, F.; Demir, F.; Bilen, M.; Okur, H. Kinetic Analysis of Thermal Decomposition of Boric Acid from Thermogravimetric Data. *Korean J. Chem. Eng.* **2006**, *23*, 736–740.
35. Searcy, A. W.; Myers, C. E. The Heat of Sublimation of Boron and the Gaseous Species of the Boron−Boric Oxide System. *J. Phys. Chem.C.* **1957**, *61*, 957–960.
36. Jacobson, N. S.; Myers, D. L. High-Temperature Vaporization of B_2O_3(l) under Reducing Conditions. *J. Phys. Chem.B.* **2011**, *115*, 13253–13260.
37. Pels, J. R.; Kapteijn, F.; Moulijn, J. A.; Zhu, Q.; Thomas, K. M. Evolution of Nitrogen Functionalities in Carbonaceous Materials During Pyrolysis. *Carbon* **1995**, *33*, 1641–1653.
38. Chisaka, M.; Iijima, T.; Ishihara, Y.; Suzuki, Y.; Inada, R.; Sakurai, Y. Carbon Catalyst Codoped with Boron and Nitrogen for Oxygen Reduction Reaction in Acid Media. *Electrochim. Acta* **2012**, *85*, 399–410.
39. Wen, Z.; Ci, S.; Zhang, F.; Feng, X.; Cui, S.; Mao, S.; Luo, S.; He, Z.; Chen, J. Nitrogen-Enriched Core-Shell Structured Fe/Fe_3C-C Nanorods as Advanced Electrocatalysts for Oxygen Reduction Reaction. *Adv. Mater.* **2012**, *24*, 1399–1404.
40. Chen, S.; Bi, J.; Zhao, Y.; Yang, L.; Zhang, C.; Ma, Y.; Wu, Q.; Wang, X.; Hu, Z. Nitrogen-Doped Carbon Nanocages as Efficient Metal-Free Electrocatalysts for Oxygen Reduction Reaction. *Adv. Mater.* **2012**, *24*, 5593–5597.
41. Yang, L.; Jiang, S.; Zhao, Y.; Zhu, L.; Chen, S.; Wang, X.; Wu, Q.; Ma, J.; Ma, Y.; Hu, Z. Boron-Doped Carbon Nanotubes as Metal-Free Electrocatalysts for the Oxygen Reduction Reaction. *Angew. Chem., Int. Ed.* **2011**, *50*, 7132–7135.
42. Qu, L.; Liu, Y.; Baek, J.-B.; Dai, L. Nitrogen-Doped Graphene as Efficient Metal-Free Electrocatalyst for Oxygen Reduction in Fuel Cells. *ACS Nano* **2010**, *4*, 1321–1326.
43. Jin, J.; Fu, X.; Liu, Q.; Zhang, J. A highly Active and Stable Electrocatalyst for the Oxygen Reduction Reaction Based on a Graphene-Supported g-C_3N_4@Cobalt Oxide Core-Shell Hybrid in Alkaline Solution. *J. Mater. Chem. A* **2013**, *1*, 10538–10545.